Partikelstoß: Kinematik

Oura

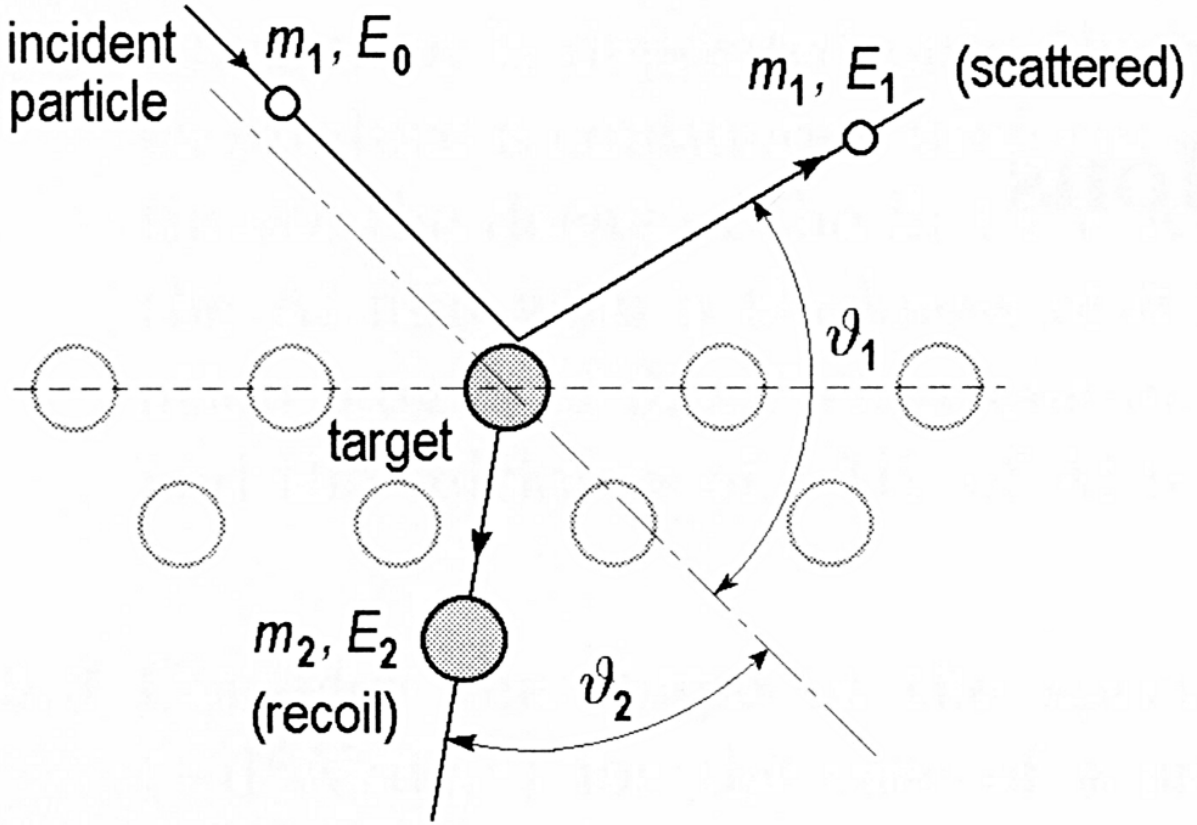

Fig. 6.1. Schematic diagram of a binary elastic collision of an incident ion (projectile) with a surface atom (target). The projectile of mass m_1 has initial energy E_0. The projectile's final scattering angle is ϑ_1 and its final energy is E_1. The target particle of the mass m_2, initially at rest, recoils at an angle ϑ_2 with energy E_2

Partikelstoß: Energie des gestreuten Atoms

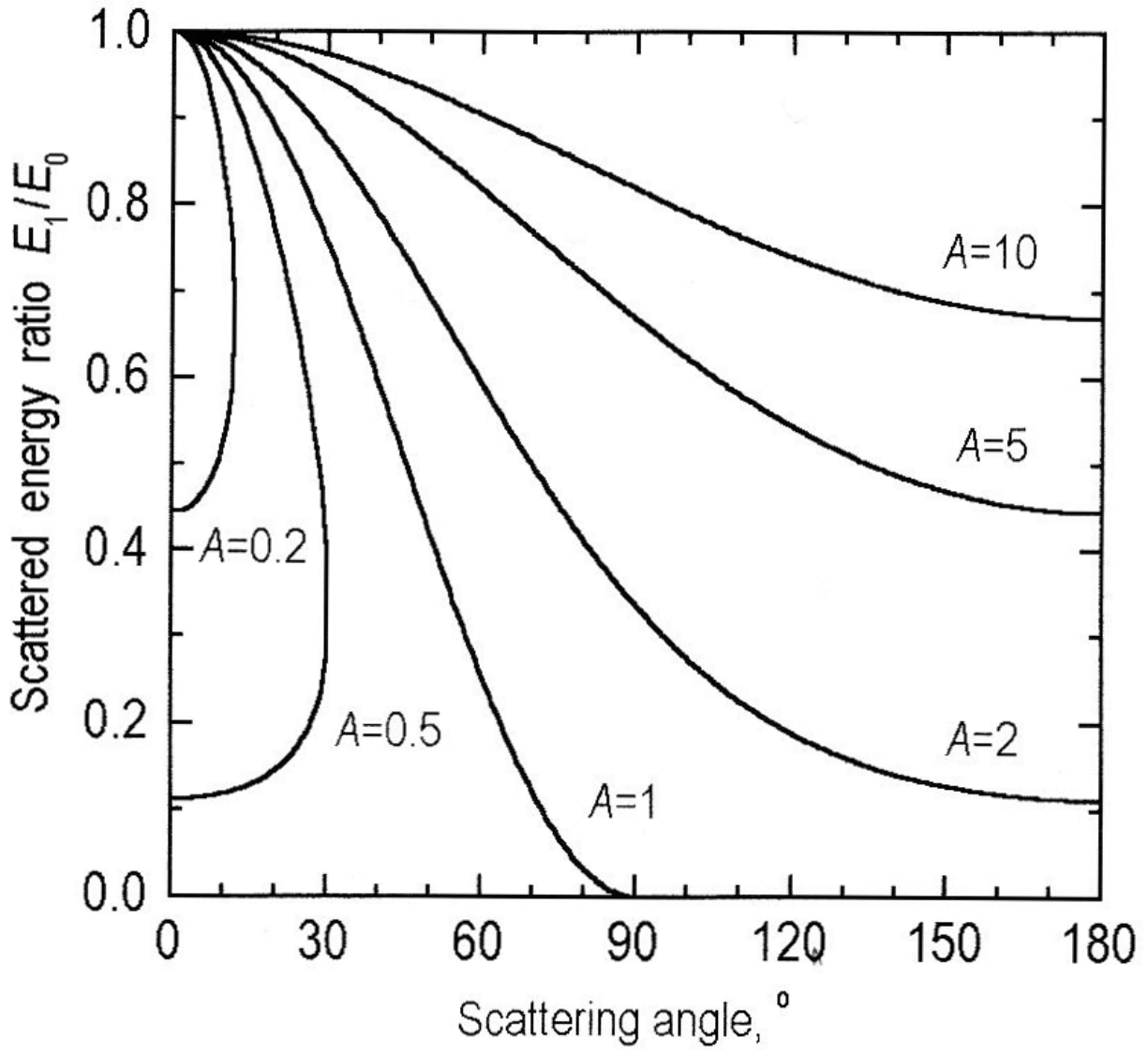

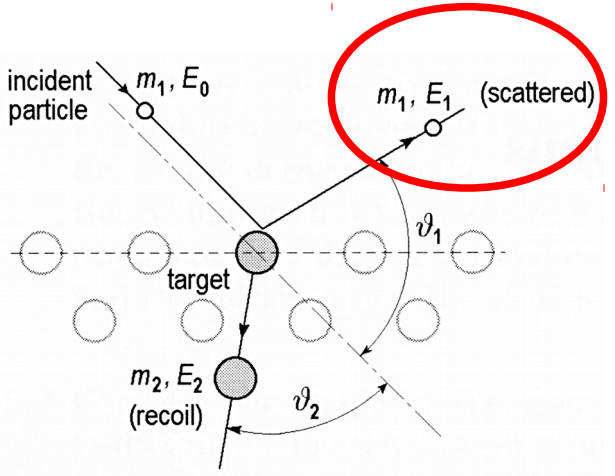

Fig. 6.2. Graphical representation of relation (6.4): Energy ratio E_1/E_0 for the scattered particles as a function of the scattering angle ϑ_1 for various values of the mass ratio $A = m_2/m_1$

Partikelstoß: Energie des Rückstoßteilchens

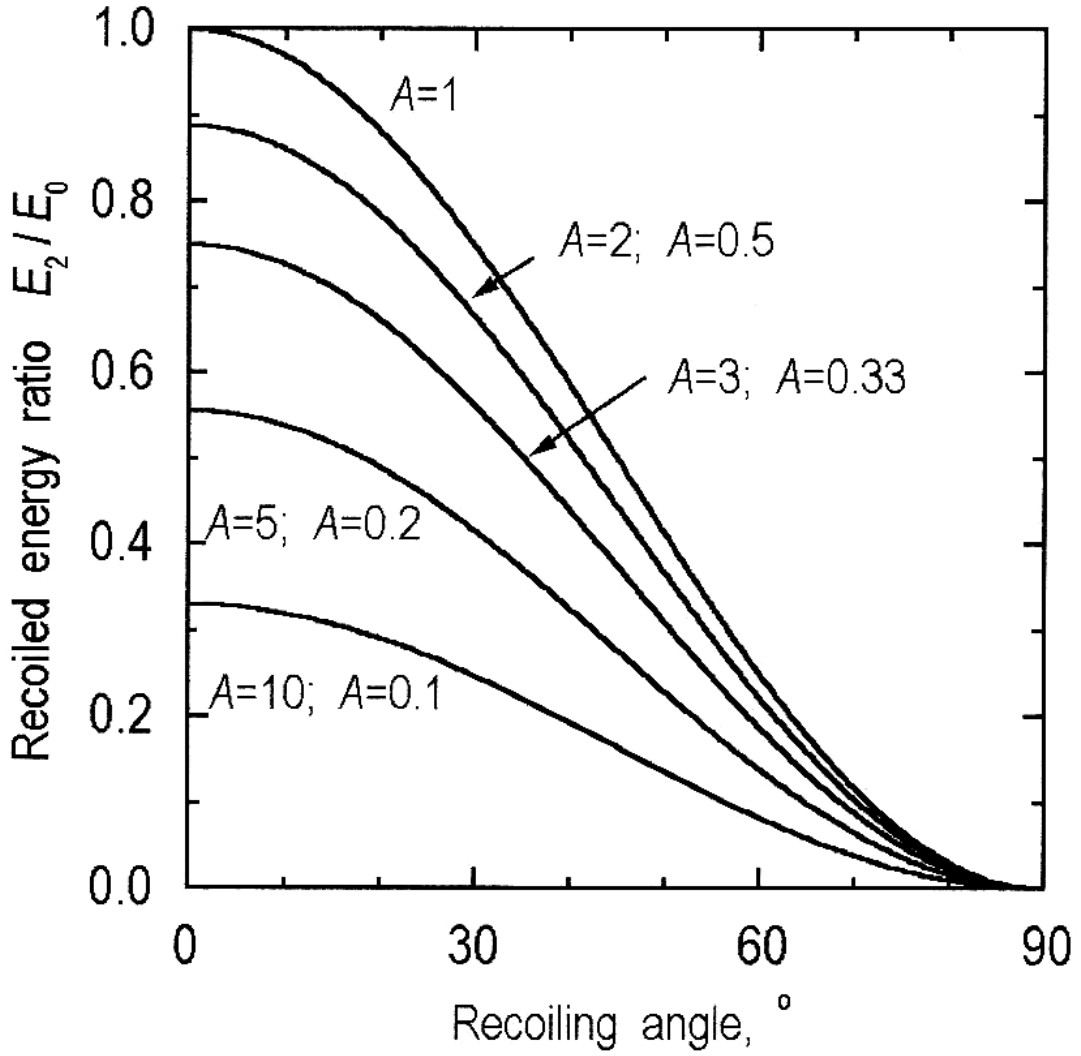

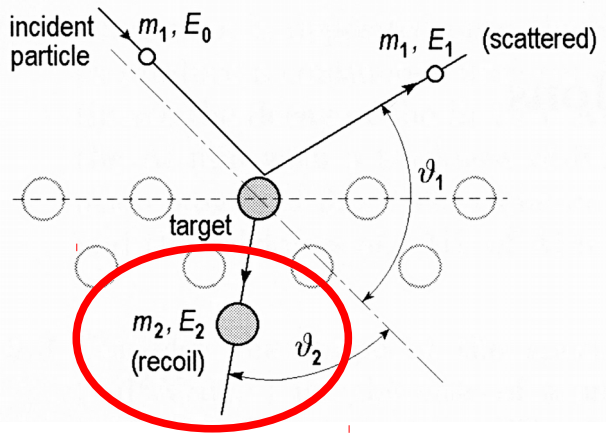

Fig. 6.3. Graphical representation of relation (6.5): Energy ratio E_2/E_0 for the recoil particles as a function of the recoiling angle ϑ_2 for various values of the mass ratio $A = m_2/m_1$. The $E_2/E_0(\vartheta_2)$ curves for A are identical to those for A^{-1}

Elementanalyse

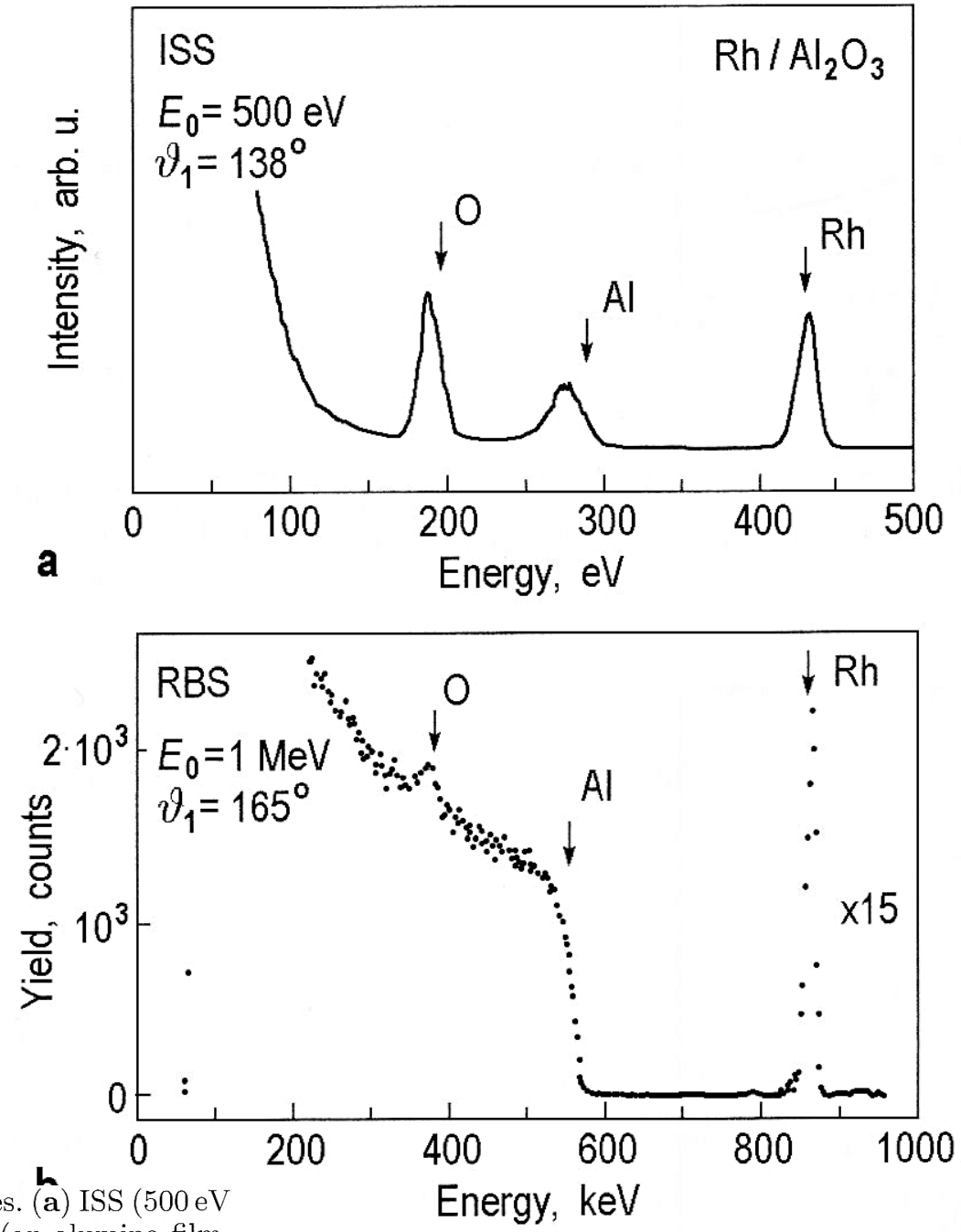

Fig. 6.4. Surface elemental analysis using ion scattering techniques. (**a**) ISS (500 eV He^+) and (**b**) RBS (1 MeV He^+) spectra of a Rh/Al_2O_3 sample (an alumina film, formed by oxidation in air, with a deposited ~1 ML of rhodium). The arrows indicate the peak positions calculated with the binary collision model (after Linsmeier et al. [6.1])

Winkelverteilung

Fig. 6.5. A schematic view of the trajectory of a scattered particle repulsed from the target nucleus by the repulsive Coulomb force. The impact parameter p and the distance of the closest approach $r_{\min}$ are denoted

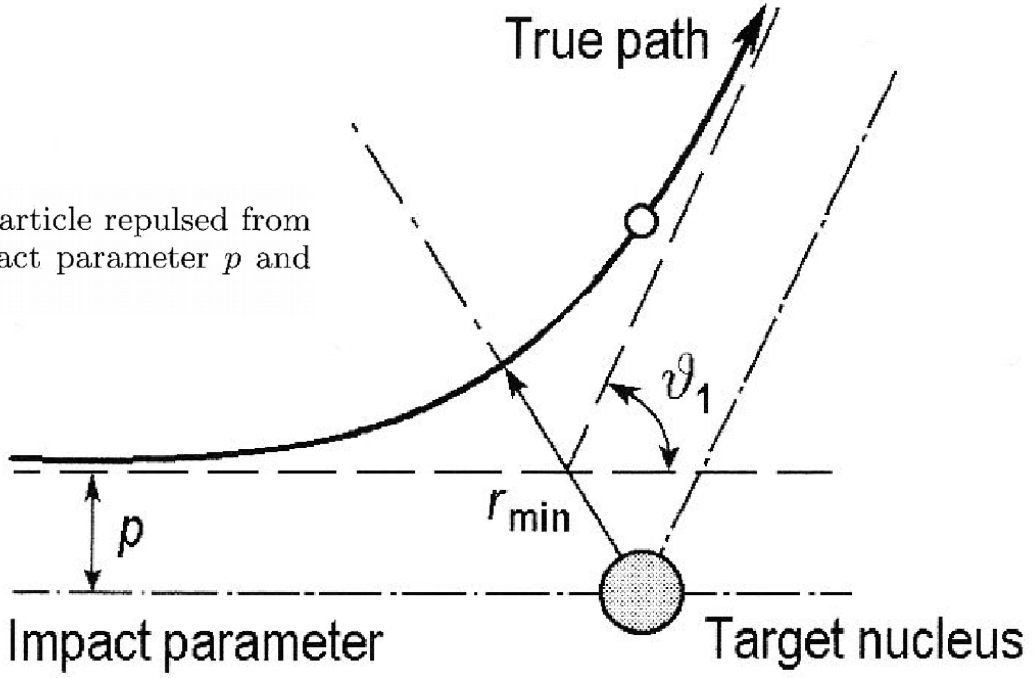

Fig. 6.6. Shadow cone formed from trajectories of projectile ions scattered from a target atom

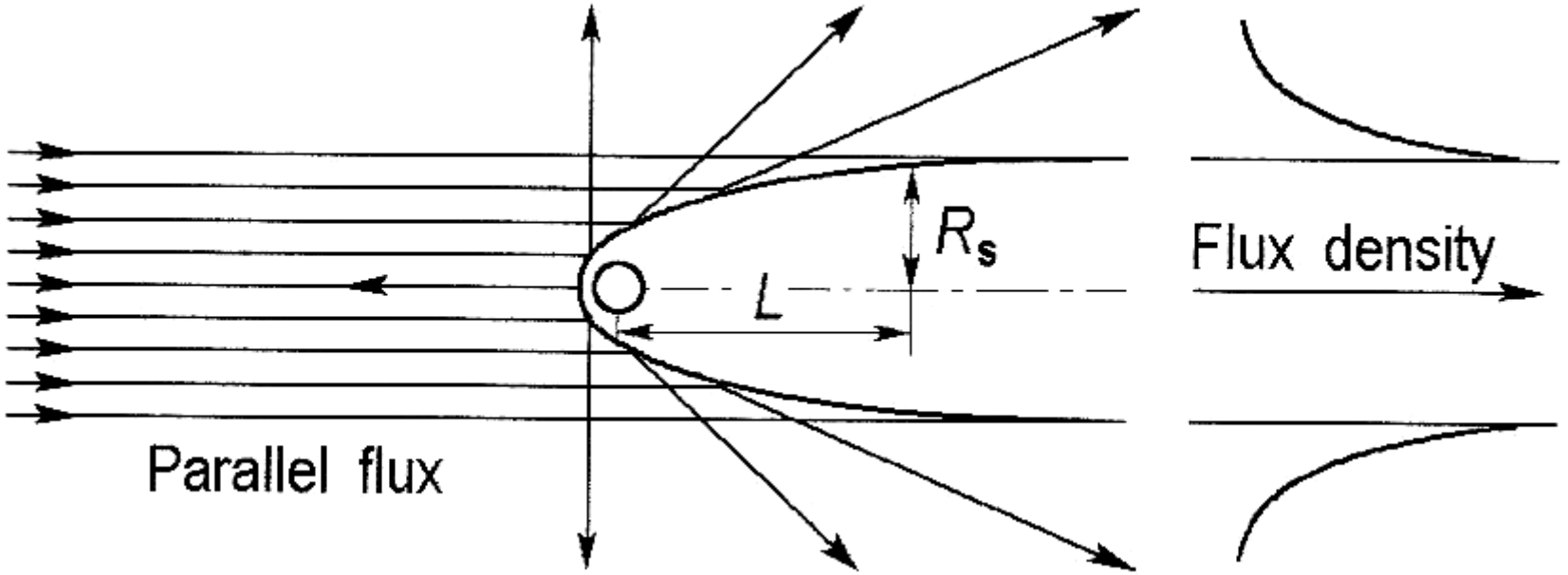

Shadowing & blocking

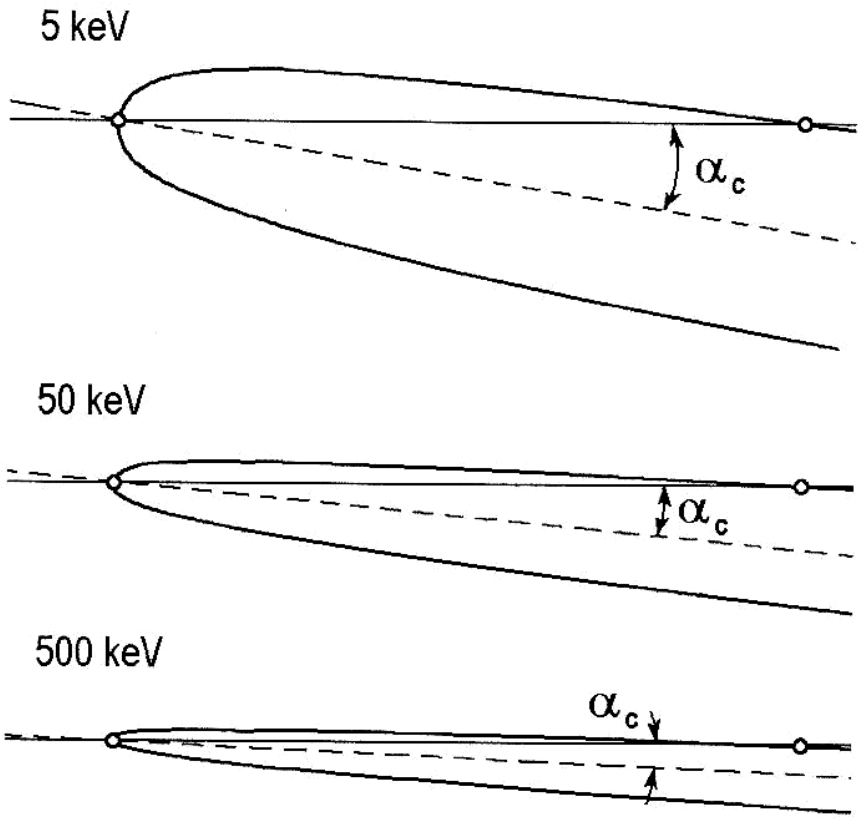

Fig. 6.7. Calculated shadow cones for Li^+ ions with energy of 5 keV, 50 keV, and 500 keV scattering from Ag atoms. The critical angles of shadowing α_c are indicated. The shadow cone width and critical angle decrease substantially with increasing ion kinetic energy (after Williams [6.3])

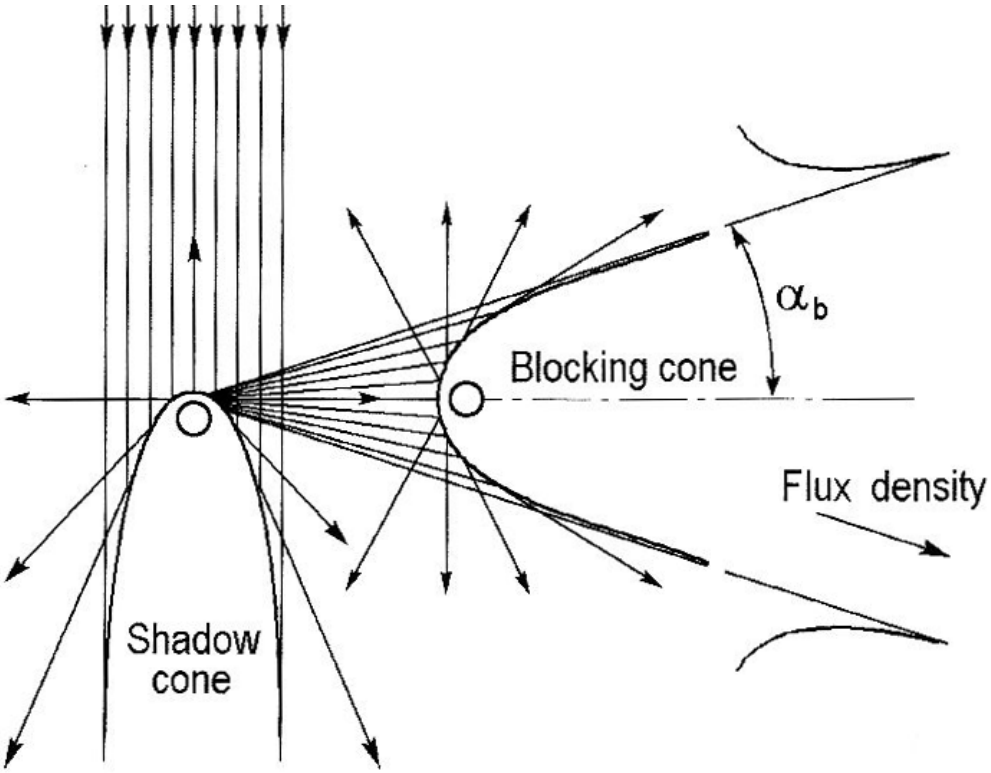

Fig. 6.8.

HEIS shadow cones

unrelaxed vs. relaxed

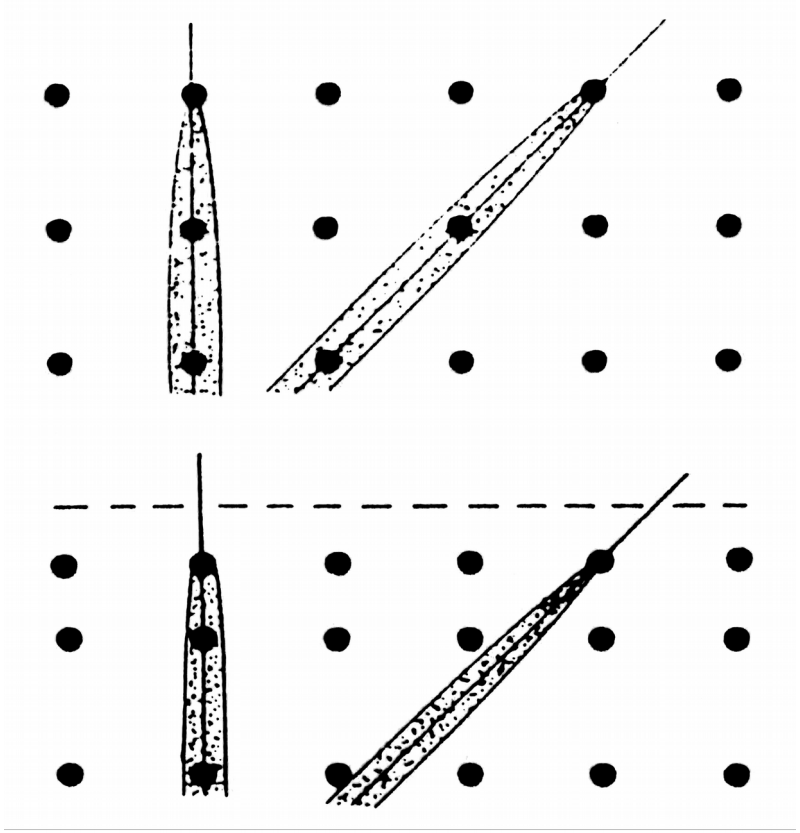

interlayer spacings

modelling → simulation

head-on scattering:

$$E' = E_0 \left(\frac{m_1 - m_2}{m_1 + m_2} \right)^2$$

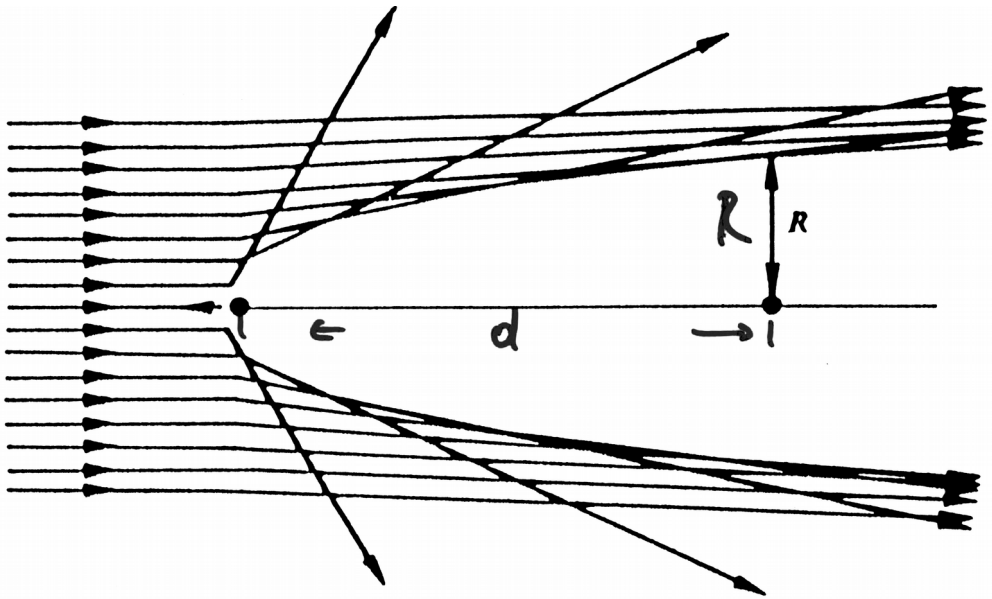

$$R = 2\sqrt{Z_1 Z_2 e^2 d / E_0}$$

Z_{ion}

Z_{TARGET}

primary beam energy

Blocking pattern of W(100)

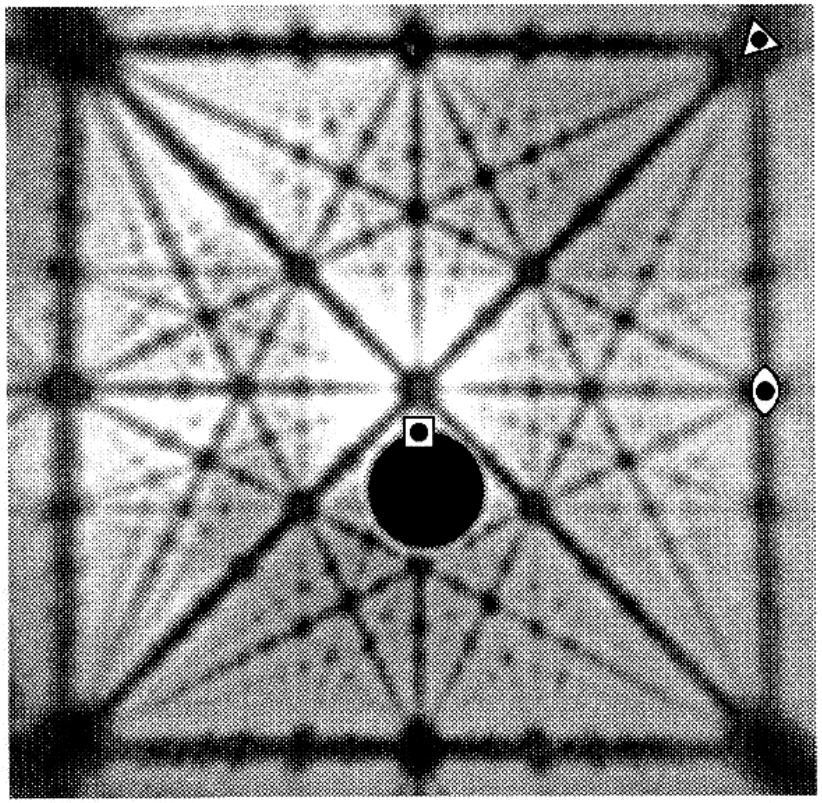

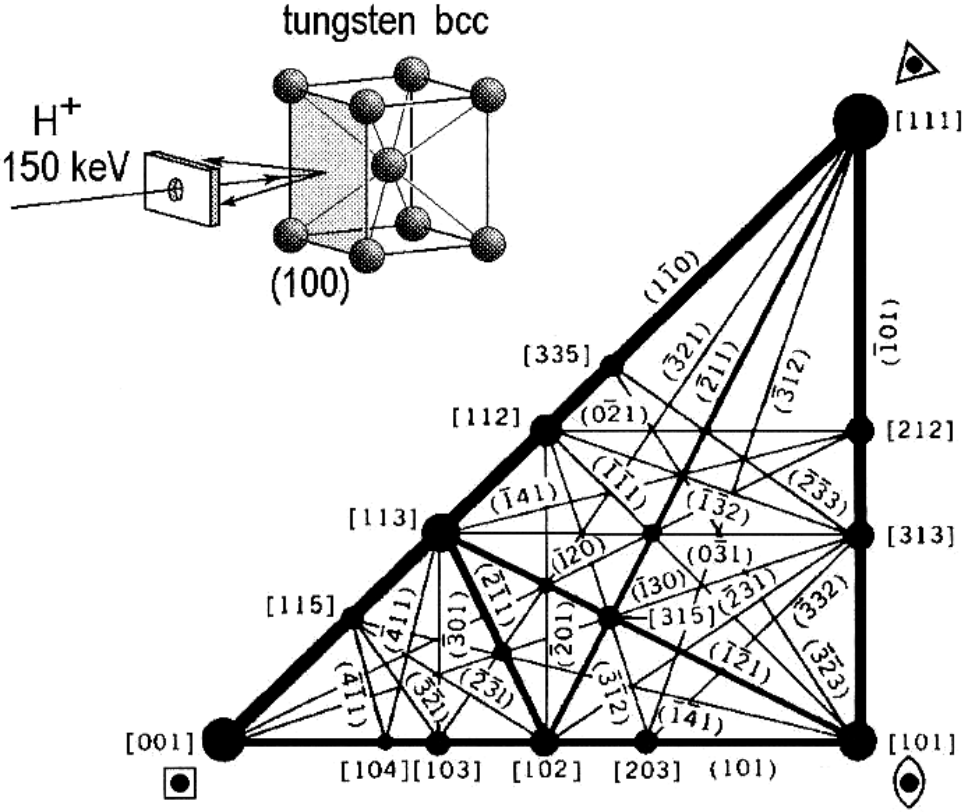

Fig. 6.9. [100] blocking pattern for 150 keV protons incident on a thick single crystal of tungsten in the non-channeling ($\sim 5°$) direction and backscattered along various high symmetry blocking directions. The angular distribution of scattered protons was monitored with radiation sensitive film. In this print from the film the black lines and spots correspond to proton-deficient regions in the film (After Barrett, Müller and White [6.5])

Channeling

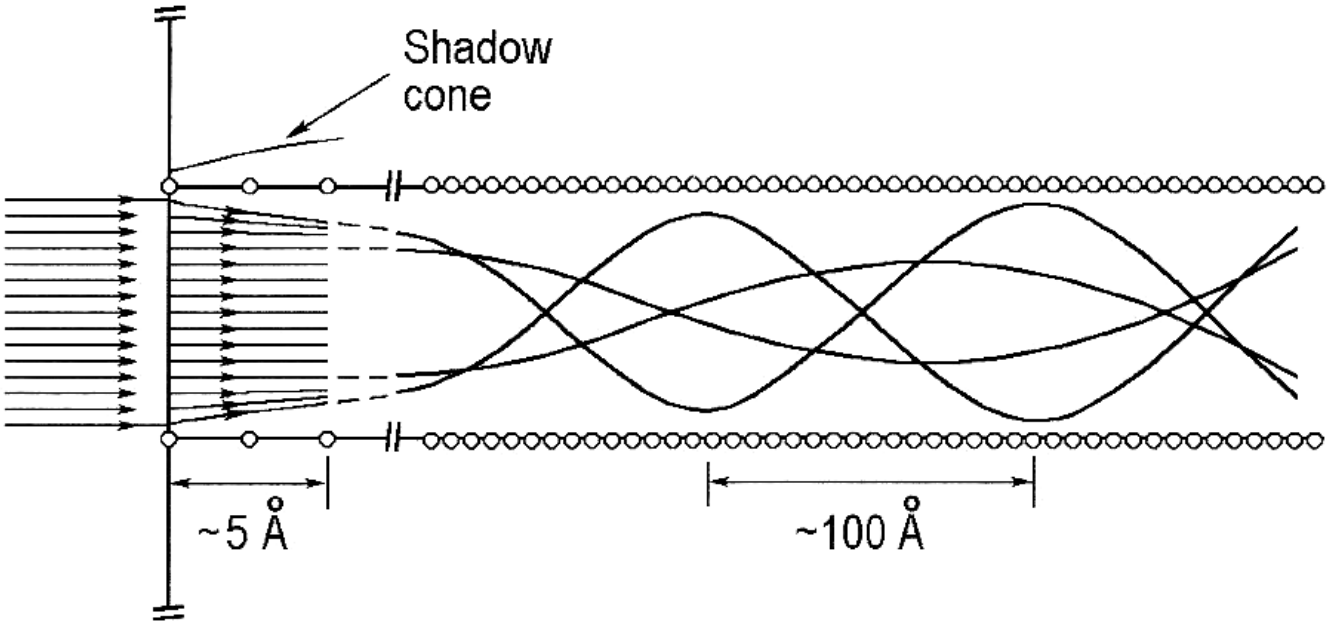

Fig. 6.10. Schematic illustration of the particle trajectories undergoing scattering at the surface and channeling within the crystal. The depth scale is compressed relative to the width of the channel in order to display the shape of the trajectories (after Feldman, Mayer and Picraux [6.6])

Role of Temperature

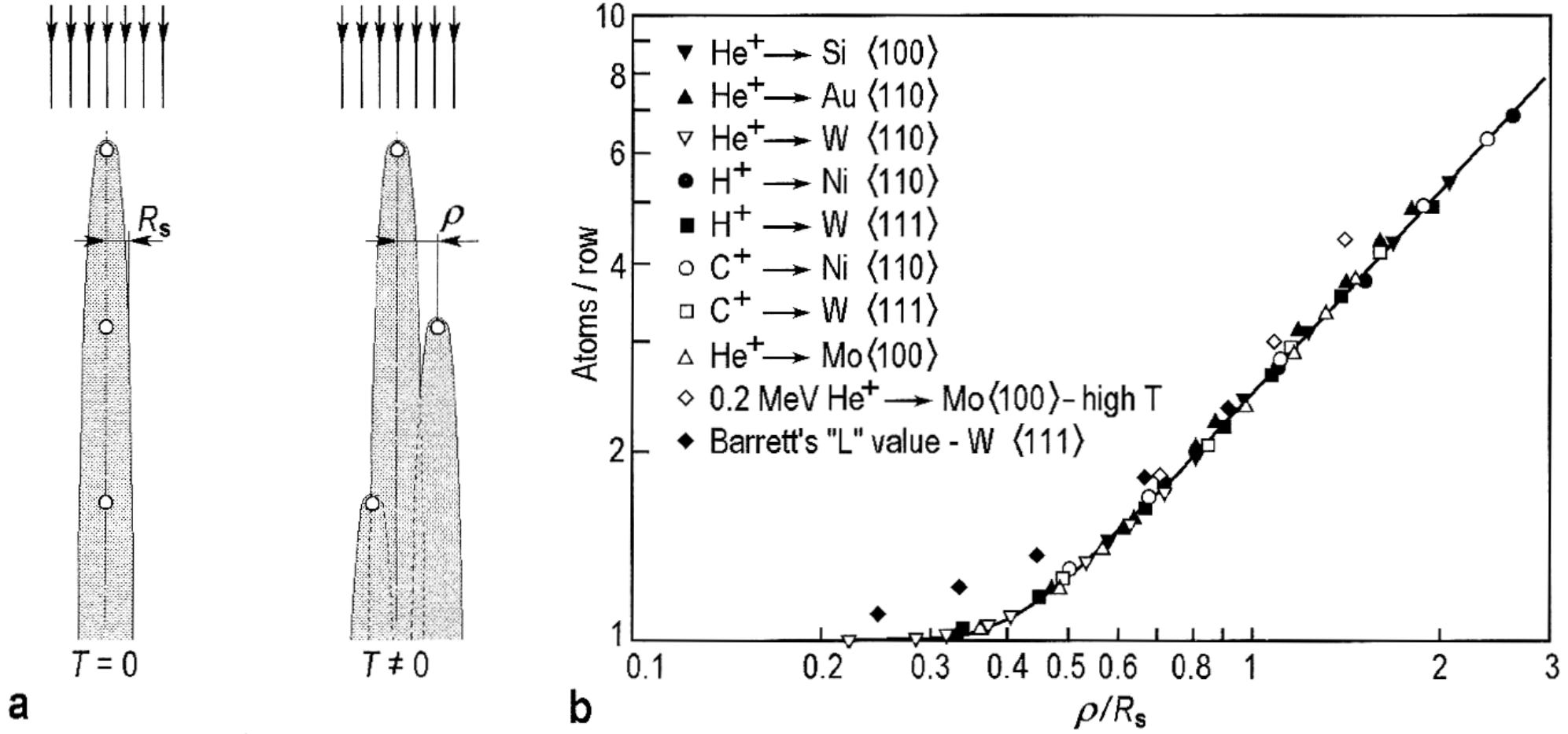

Fig. 6.23. (**a**) Schematic illustration of the shadow effect along an atomic row at zero and non-zero temperature. R_s indicates the radius of the shadow cone at interatomic distance, ρ is the amplitude of the thermal atomic vibrations. (**b**) Number of atoms per row visible to the incident ion beam as a function of ρ/R_s calculated for a large set of ion–target combinations (after Stensgaard et al. [6.18])

Surface peak

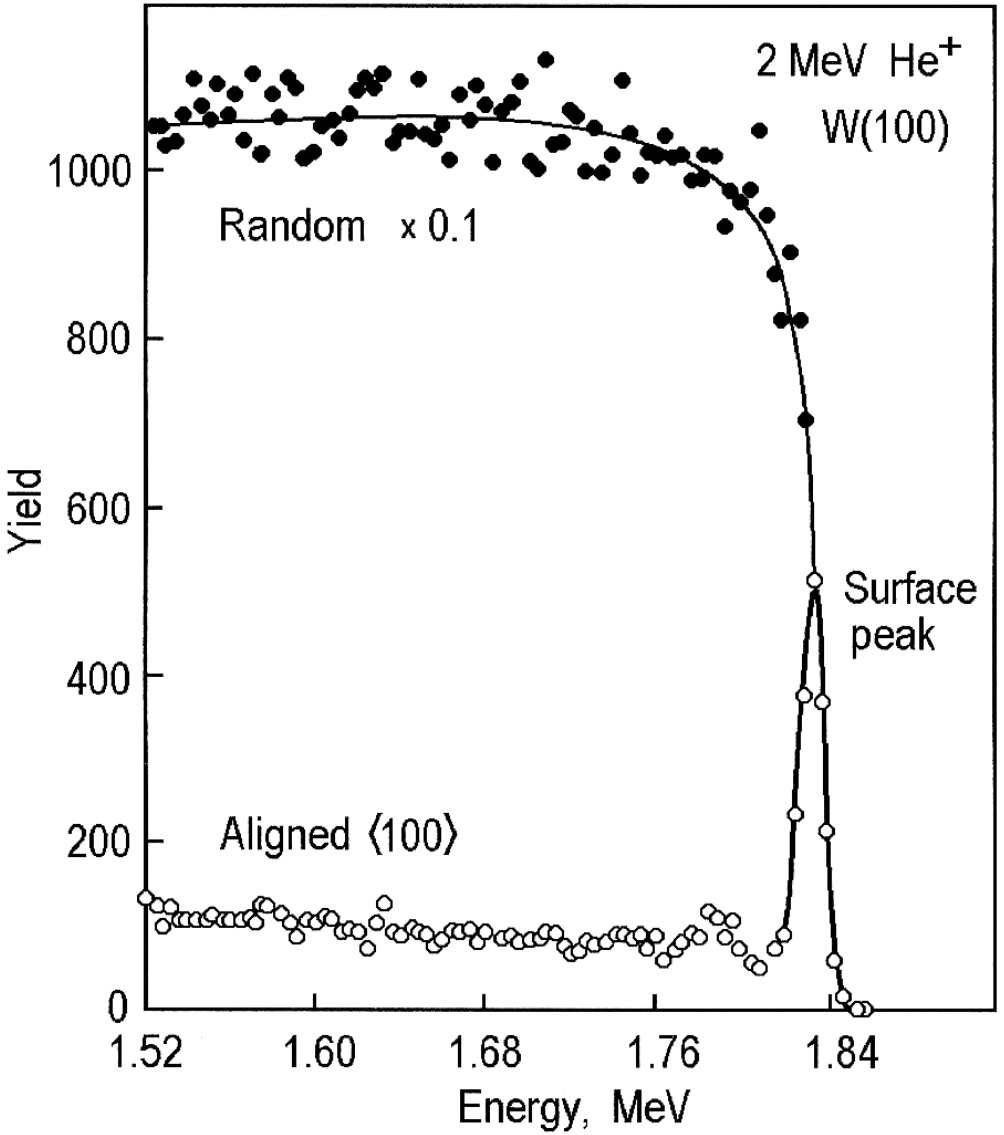

Fig. 6.24. RBS spectra for 2 MeV He^+ ions incident on W along the ⟨100⟩ axial direction ("aligned" spectrum, open circles) and in the non-channeling direction ("random" spectrum, closed circles) (after Feldman et al. [6.19])

Idealized backscattering patterns

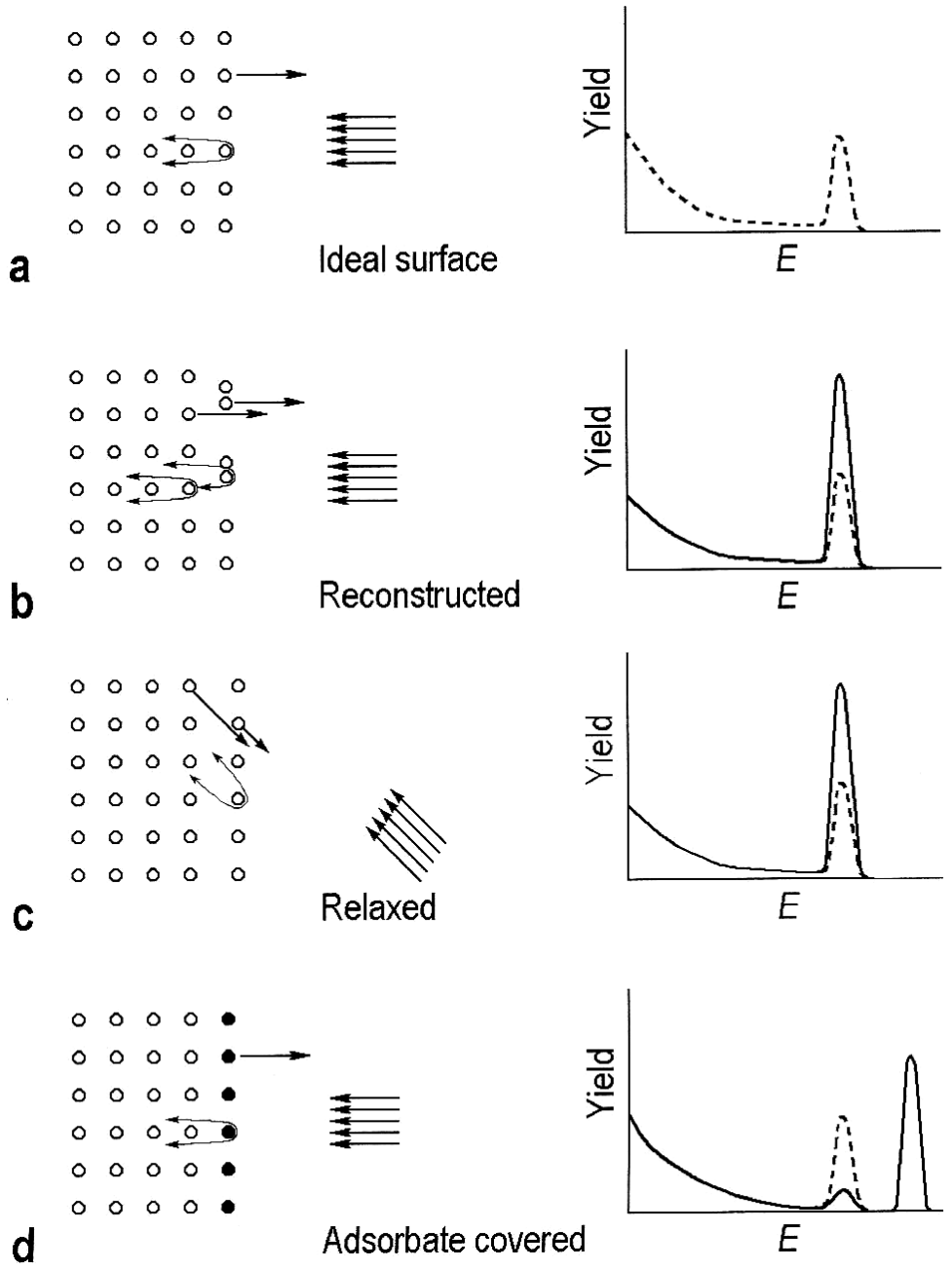

Fig. 6.25. Schematic diagram of the expected backscattering signal from various surface structures: (**a**) ideal crystal surface; (**b**) surface with lateral reconstruction; (**c**) surface relaxed in the normal direction; (**d**) surface with an adsorbate layer (after Feldman et al. [6.6])

Separating bulk & surface

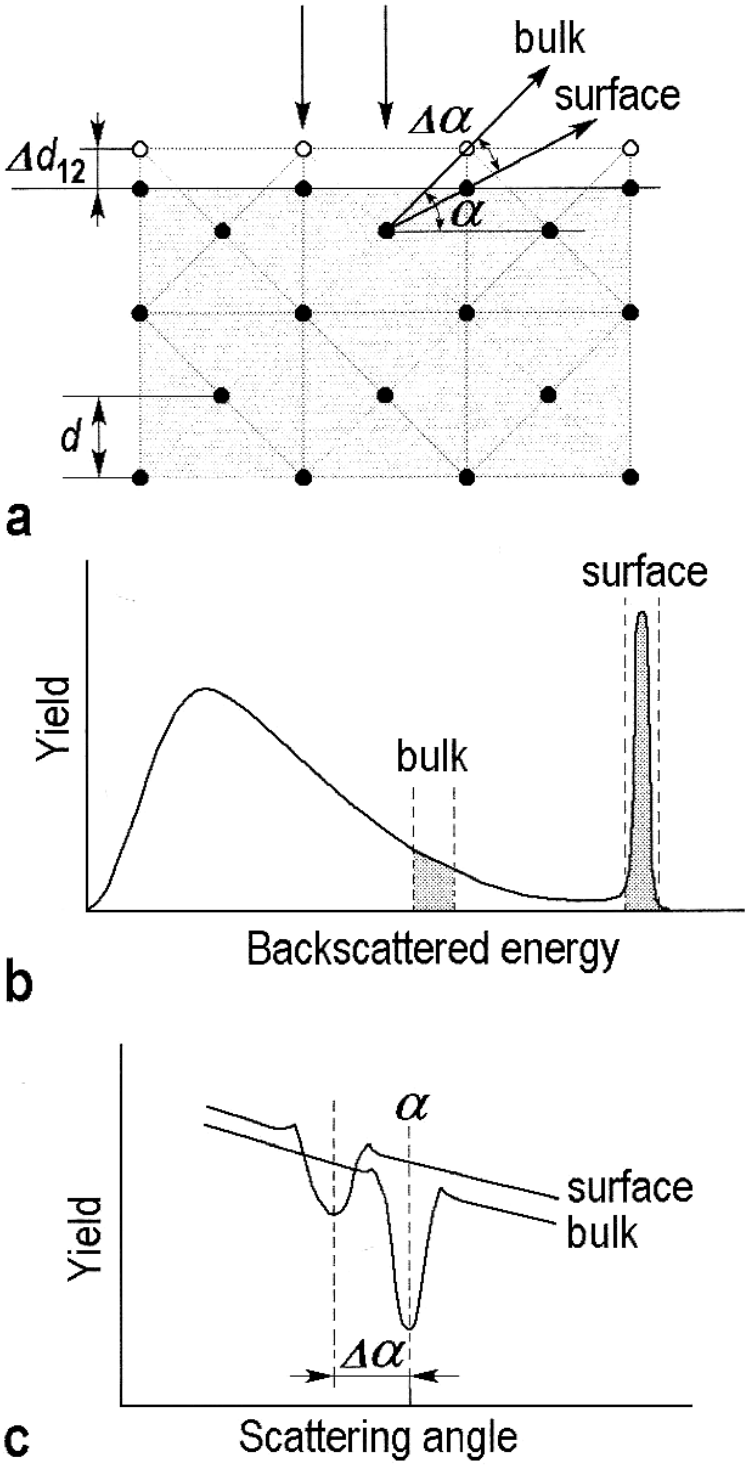

Fig. 6.26. Schematic illustration of the method to study surface relaxation. In scheme (**a**) actual positions of atoms are shown by closed circles, while open circles show the positions of the atoms in the unrelaxed ideal first atomic layer. Due to relaxation by Δd_{12}, the surface blocking minimum direction is tilted by $\Delta\alpha$ with respect to the bulk axis. In the experiment, $\Delta\alpha$ is measured by plotting the surface and bulk scattering intensities (**b**) as a function of scattering angle (**c**). Δd_{12} is calculated from $\Delta\alpha$ according to (6.15) (after Turkenberg et al. [6.20])

A spectacular example: Pb(110)

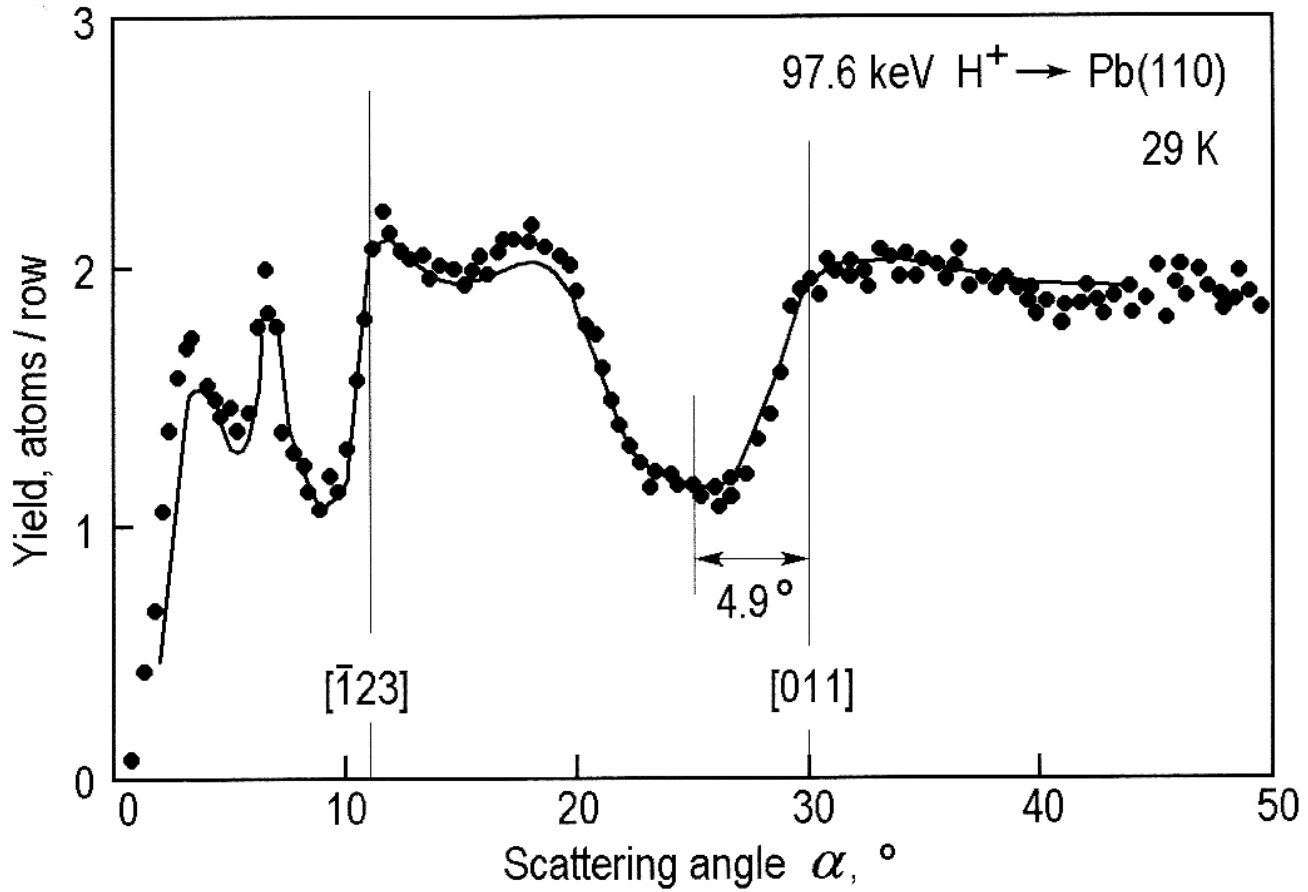

Fig. 6.27. Angular dependence of the surface backscattering peak from a Pb(110)1×1 surface at 29 K. The blocking minimum at 25.1° is shifted from the bulk [011] direction due to the inward relaxation of the outermost atomic layer of the crystal. The best fit of Monte Carlo simulations (solid curve) is obtained for $\Delta d_{12}/d = -(17.2 \pm 0.5)\%$ and $\Delta d_{23}/d = +(8.0 \pm 2.0)\%$ (after Frenken et al. [6.21])

Layered materials

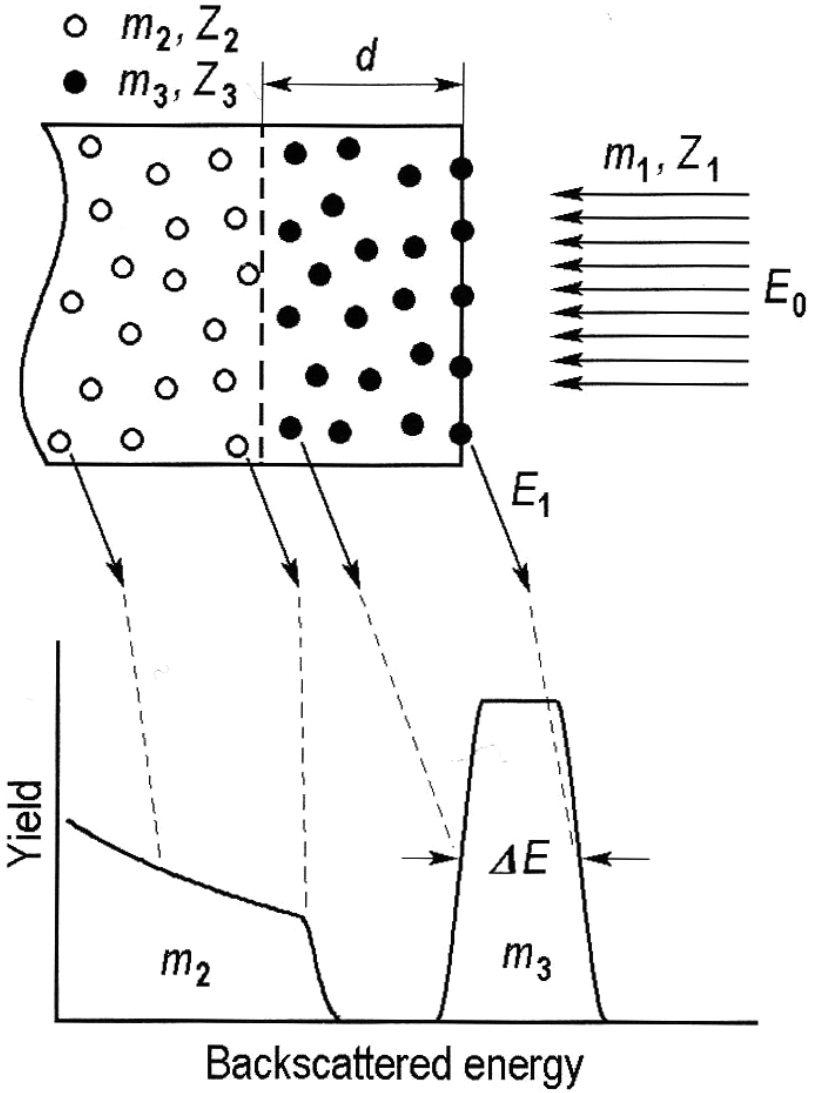

Fig. 6.28. Schematic diagram of the energy spectrum of ions (m_1, Z_1, E_0) scattered from a sample composed of a substrate (m_2, Z_2) and a film (m_3, Z_3) of thickness d. For simplicity, both film and substrate are assumed to be amorphous to neglect the structural effects. (after Feldman et al. [6.6])

Ionen zerstäuben

Ionenzerstäuben (sputtering)

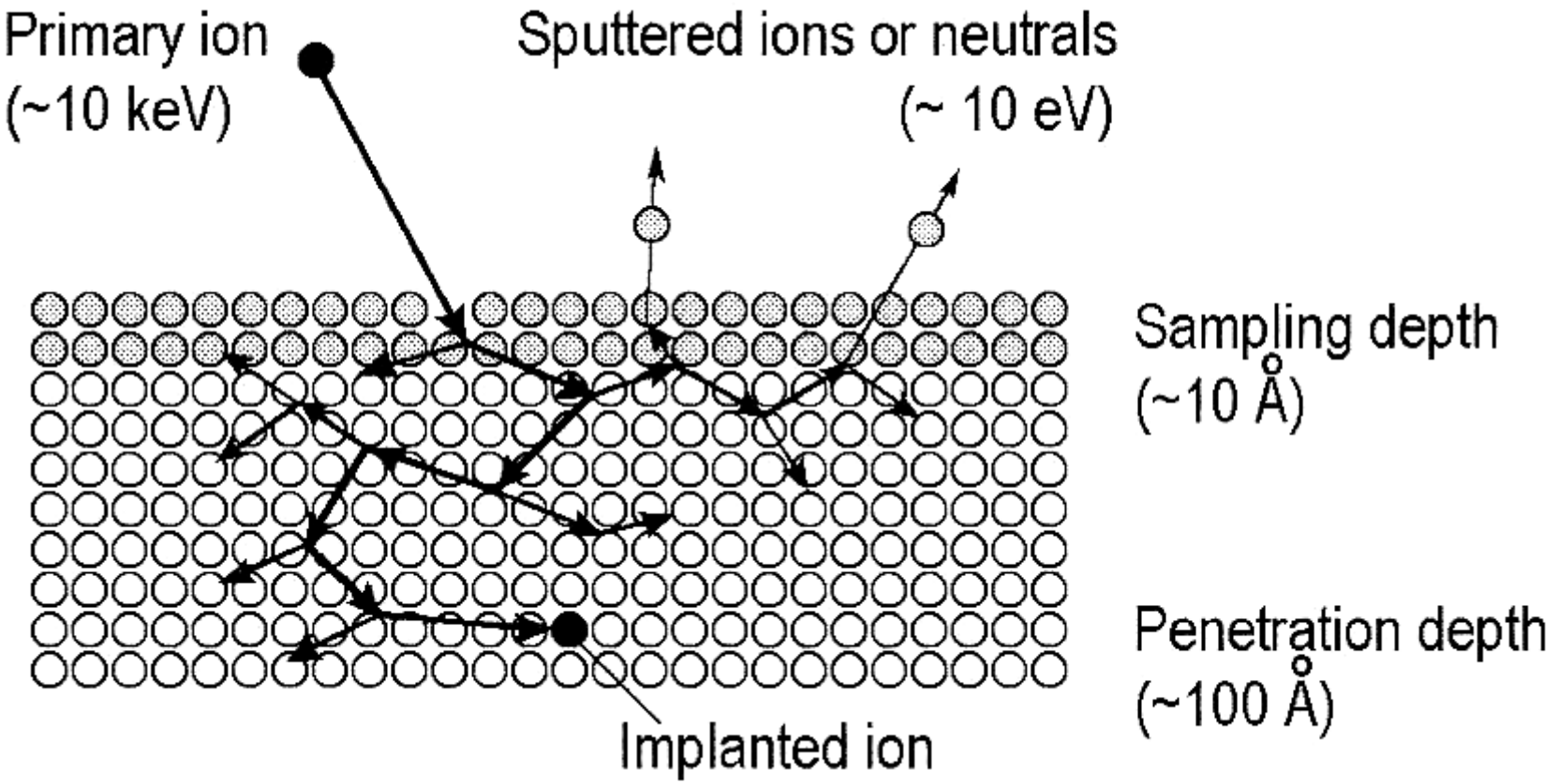

Fig. 6.11. Schematic representation of the processes taking place upon penetration of the impinging ion into the solid. The cascade of collisions results in ion implantation and sputtering of surface species. The shown numerical values provide a feeling for the orders of magnitude for the ion penetration depth, escape depth, and energy of sputtered species when bombarding the surface with 10 keV ions

Ionenzerstäuben: Primärenergie

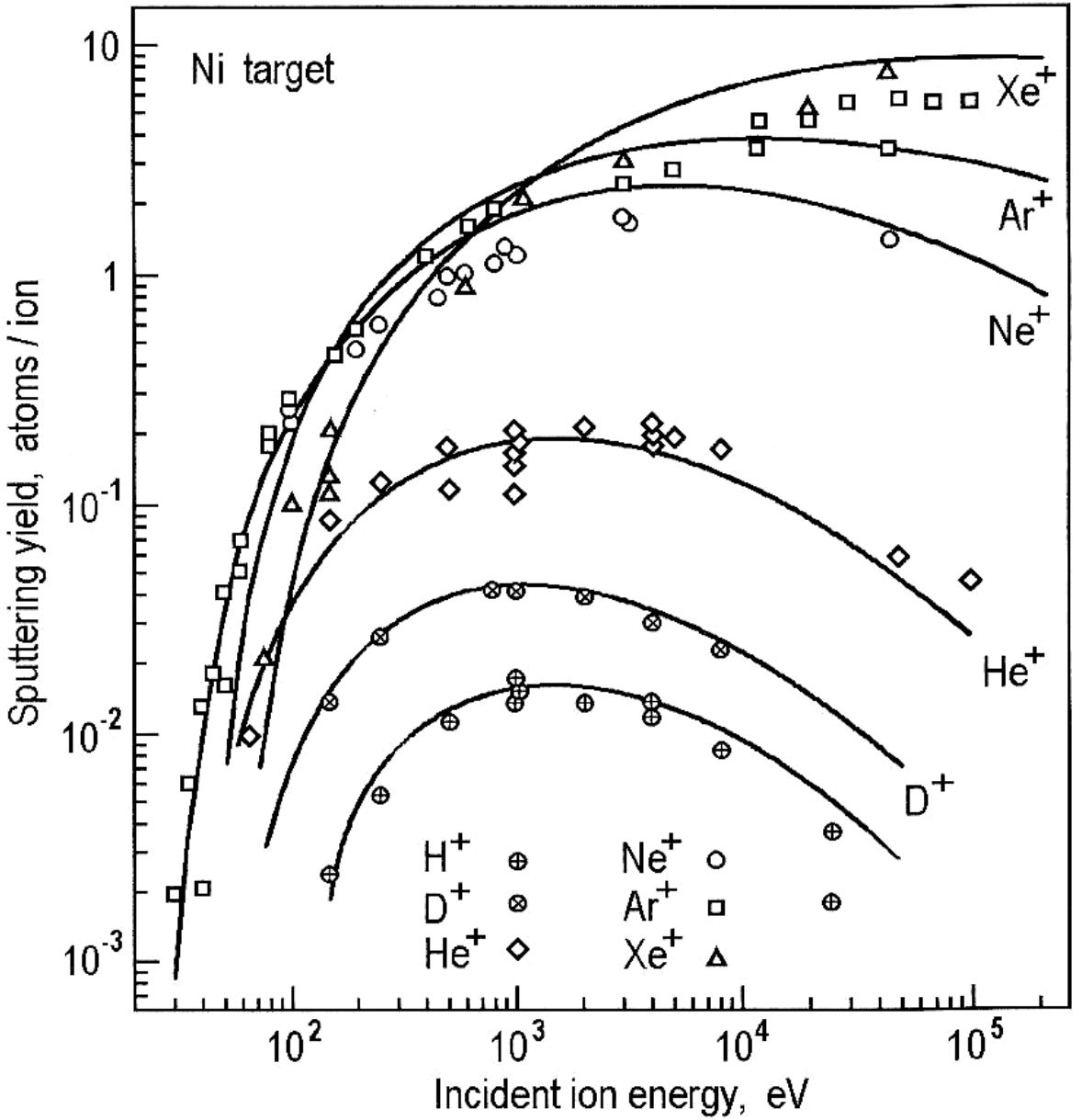

Fig. 6.12. Sputtering yield as a function of the primary ion energy for bombardment of a polycrystalline Ni sample by various ions at normal incidence (after Ziegler et al. [6.7])

Ionenzerstäuben: Einfallswinkel

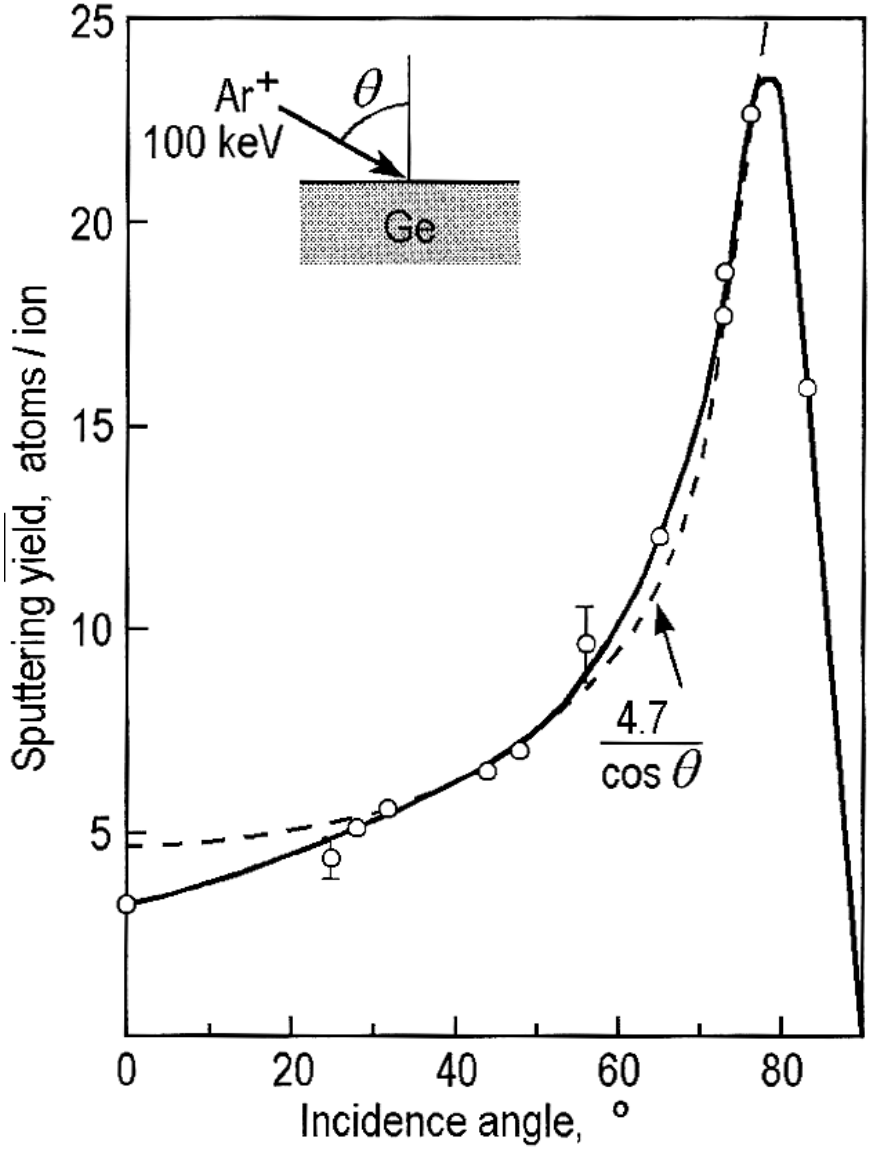

Fig. 6.13. Variation of the sputtering yield with ion incidence angle θ for 100 keV argon bombardment of germanium which amorphizes readily under ion impact (after Wilson et al. [6.8])

Secondary Ion Mass Spectrometry (SIMS)

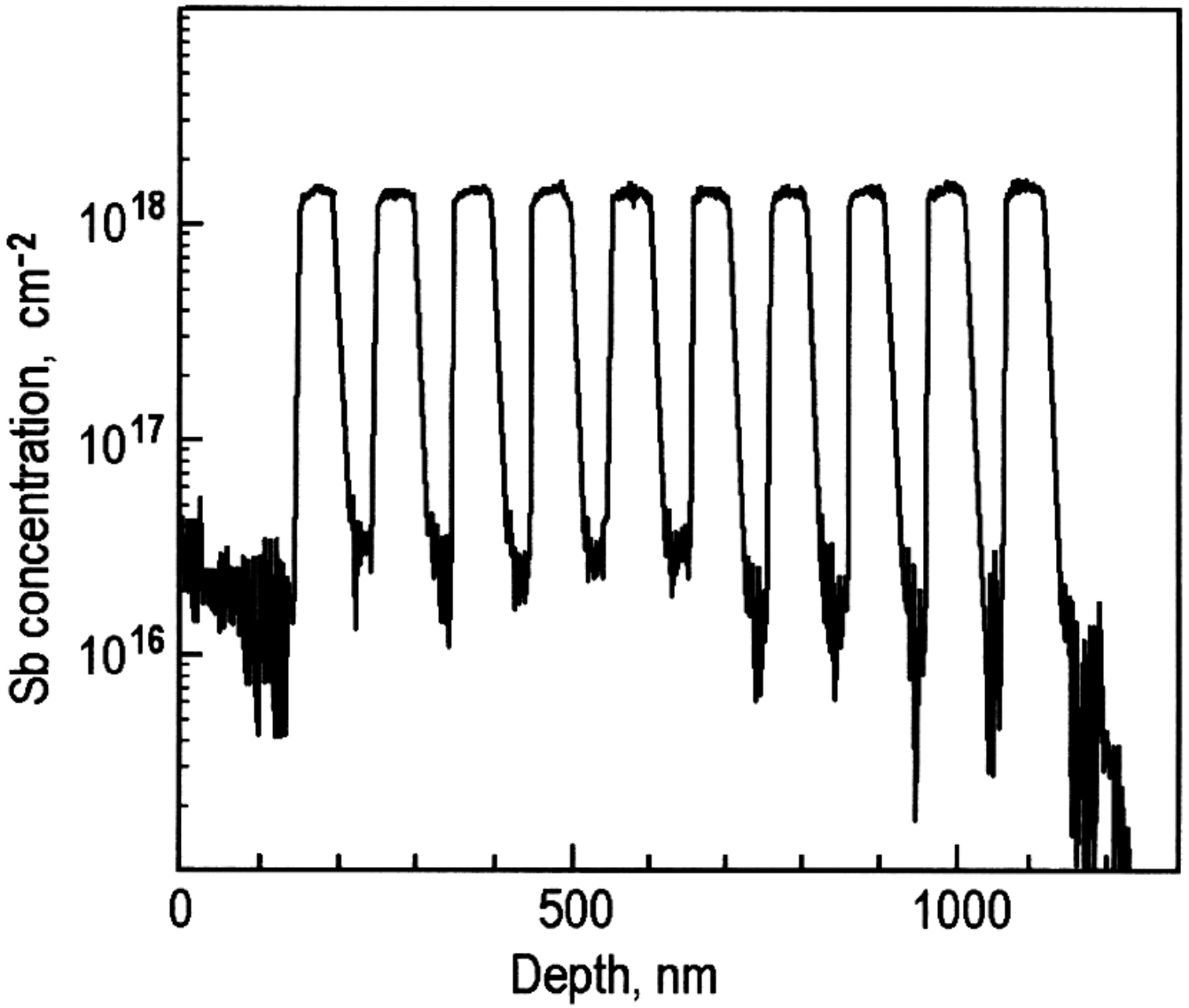

Fig. 6.31. SIMS depth profile of Sb in the modulation-doped silicon multilayer structure grown by molecular beam epitaxy (after Casel et al. [6.25])

Elektronische Prozesse

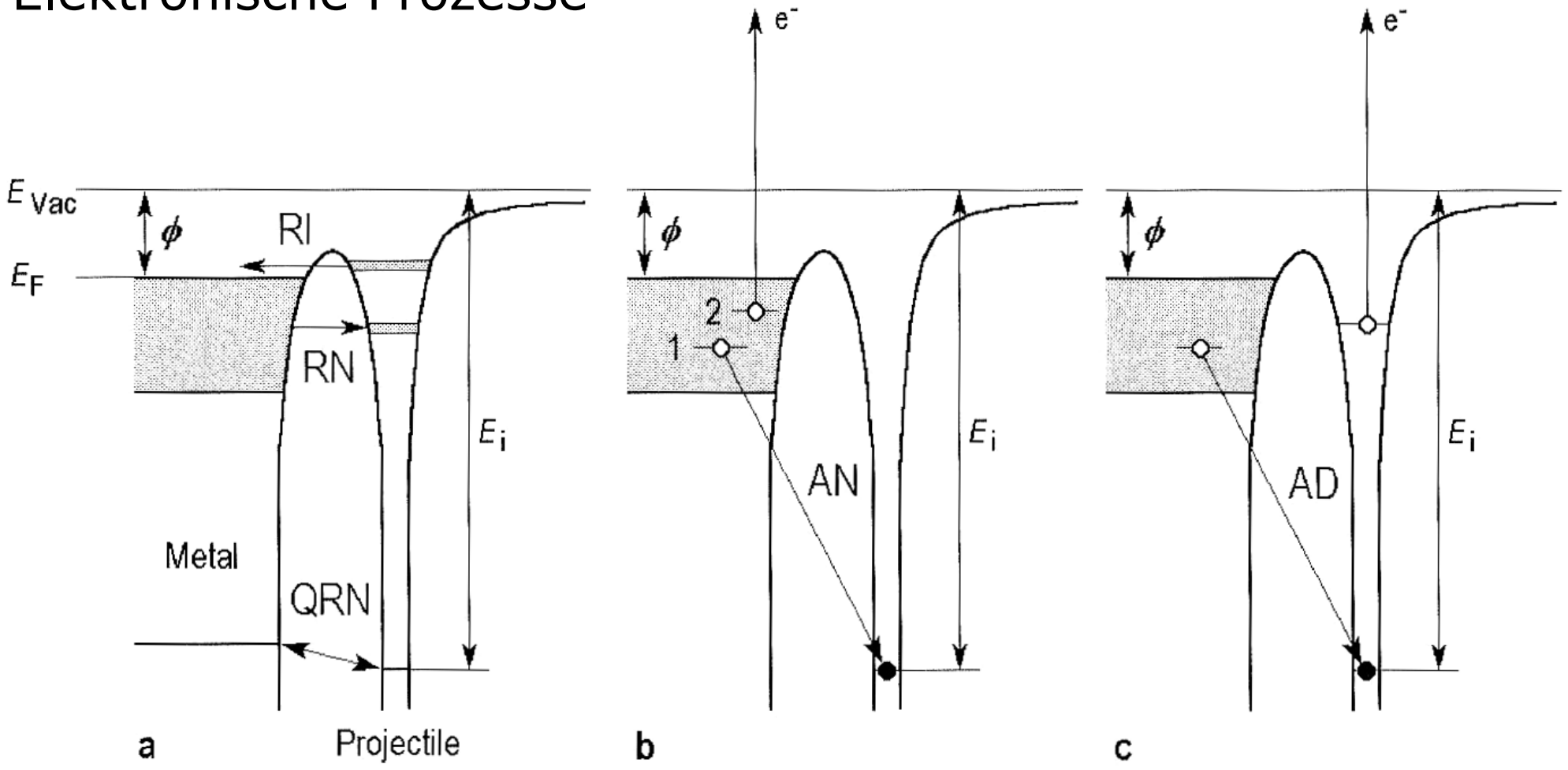

Fig. 6.14. Schematic energy level diagrams showing the charge exchange processes between a solid and an ion. (**a**) One-electron processes are represented by resonance neutralization (RN), resonance ionization (RI), and quasi-resonant neutralization (QRN). Two-electron processes are represented by (**b**) Auger neutralization (AN) and (**c**) Auger de-excitation (AD). E_{F} is the Fermi energy of the solid, E_{Vac} is the vacuum energy, $\phi = E_{\mathrm{Vac}} - E_{\mathrm{F}}$ is the work function of the solid, and E_{i} is the ionization energy of the ion (after Hagstrum [6.9])

Oscillatory neutralization

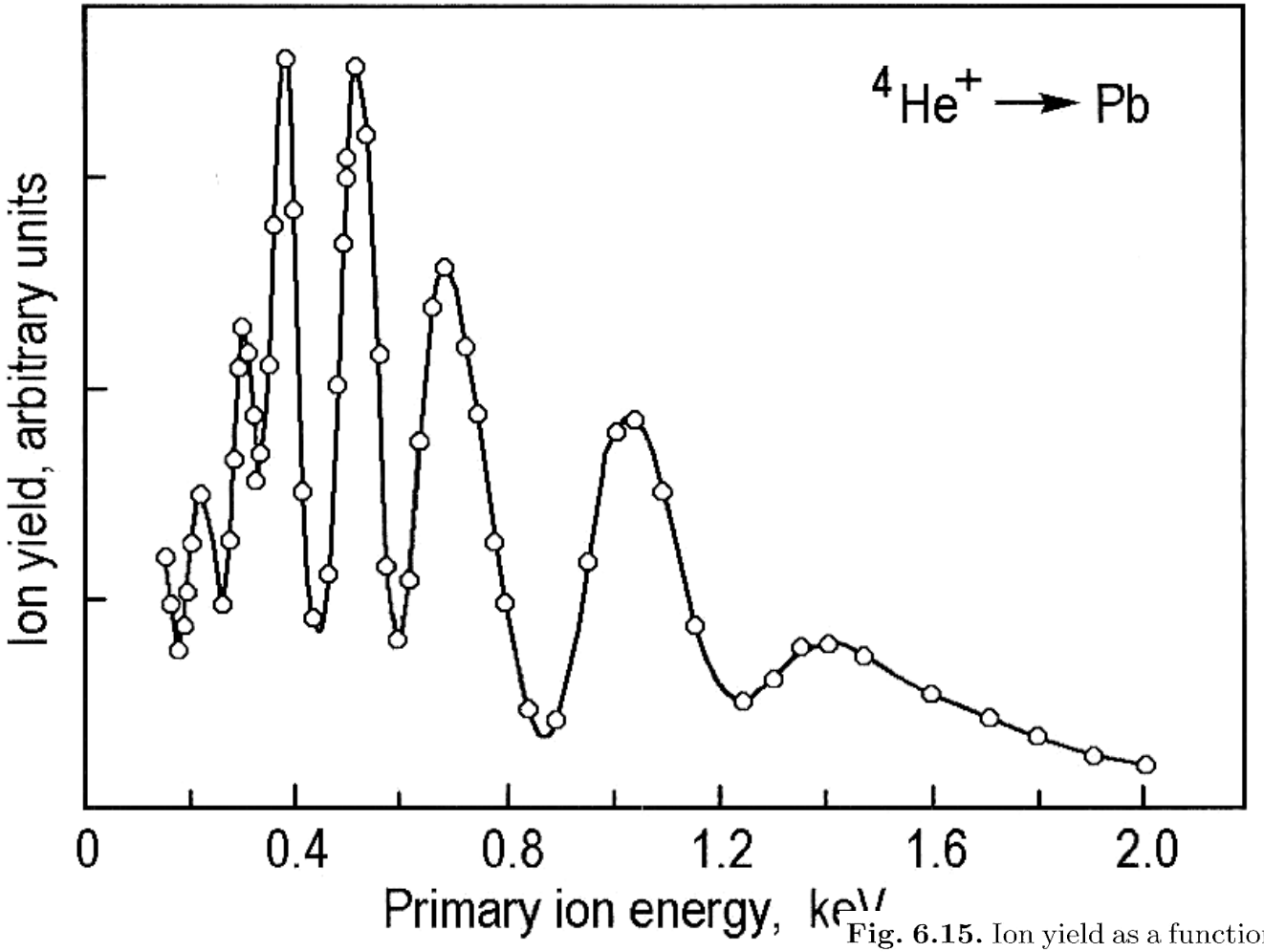

Fig. 6.15. Ion yield as a function of the primary ion energy for $^4He^+$ scattering from Pb targets. The oscillatory behavior of the ion yield is explained by *quasi-resonant neutralization processes* as follows. Electron exchange processes are dependent upon the interaction time, which is a function of the primary ion velocity (energy). For a sufficiently high ion velocity, the collision time is so short that the electron has just enough time to transfer to the incident ion; the ion then scatters away, neutralized. For a somewhat lower ion velocity, there will be sufficient time for the electron to transfer to the incident ion and back again to its parent atom, resulting in no neutralization. For progressively lower ion velocities, a succession of electron-exchange events takes place. The minima in the ion yield correspond to those ion velocities (collision times) where charge exchange results in scattering of a neutral. The period of oscillation is constant when the data are plotted against inverse velocity of the incident ion (after Erickson and Smith [6.10])